

A dynamic circuit for the honeycomb Floquet code

Jahan Claes

In the typical implementation of a quantum error-correcting code, each stabilizer is measured by entangling one or more ancilla qubits with the data qubits and measuring the ancilla qubits to deduce the value of the stabilizer. Recently, the dynamic circuit approach has been introduced, in which stabilizers are measured without ancilla qubits. Here, we demonstrate that dynamic circuits are particularly useful for the Floquet code. Our dynamic circuit increases the timelike distance of the code, automatically removes leakage, and both significantly increases the threshold and lowers the logical error rate compared to the standard ancilla-based circuit. At a physical error rate of 10^{-3} , we estimate a nearly $3\times$ reduction in the number of qubits required to reach a 10^{-12} logical error rate.

INTRODUCTION

Quantum error correction (QEC) will be necessary to reach the logical error rates required for long quantum algorithms. QEC is performed by repeatedly measuring a set of Pauli operators, known as stabilizers, that detect the presence of errors [1–5]. Typically, stabilizers of a QEC code are measured using one or more ancilla qubits that are entangled with the data qubits of the code [6–9]. Recently, the idea of *dynamic* or *morphing* stabilizer measurement circuits has been introduced [9–13], in which stabilizers of the code are measured without ancilla qubits. Instead, to measure a Pauli operator $P = \otimes_i P_i$, we run a short quantum circuit U that sends $P \mapsto P_{i^*}$, where P_{i^*} is a single-qubit operator which can then be directly measured. This approach may use fewer qubits [12] or couplers [10, 13], but it may also reduce the distance of the code [9].

The Floquet code is a QEC code defined on the honeycomb lattice, in which stabilizers are given by the product of two-qubit Pauli gauge measurements [5]. In previous work, each two-qubit measurement was performed using an ancilla qubit [14, 15]. In this work, we demonstrate that the Floquet code is particularly amenable to the dynamic circuit approach. We present a dynamic circuit with several notable differences compared to the standard ancilla-based circuit:

- The dynamic circuit removes leakage by measuring each qubit after four layers of two-qubit gates. It is not obvious how to do this in the standard circuit, as there is no Floquet equivalent of the “walking surface code” [10]. (✓)
- For an $L_1 \times L_2$ patch of code, the dynamic circuit uses $L_1 L_2$ qubits and $\frac{3}{2} L_1 L_2$ couplers, compared to $\frac{5}{2} L_1 L_2$ qubits and $3 L_1 L_2$ couplers in the standard circuit. (✓)
- To reach a distance d , the dynamic circuit requires $(L_1, L_2) = (2d, 3d)$ compared to $(d, 2d)$ in the standard circuit. (✗)
- To achieve a timelike distance d_t , the dynamic circuit requires measuring a complete set of two-body operators d_t times, compared to $\frac{4}{3} d_t$ in the stan-

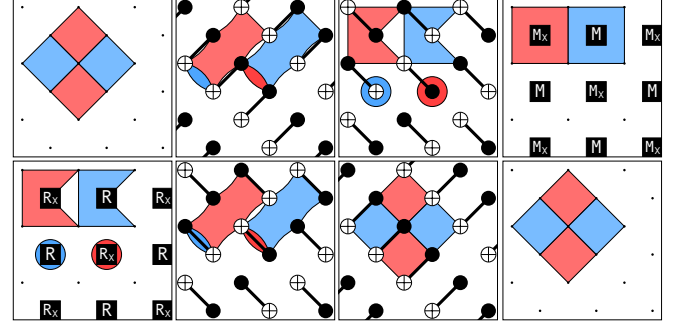


FIG. 1. The dynamic circuit for measuring the stabilizers of the rotated surface code. The state of four neighboring stabilizers is tracked through the circuit, with Z (X) stabilizers in blue (red). Half the stabilizers shrink and are measured, while the neighboring stabilizers grow.

dard circuit. (✓)

- The threshold of the dynamic circuit is .29% under circuit-level depolarizing noise, compared to .21% in the standard circuit. (✓)
- The dynamic circuit has a much lower logical error rate than the standard circuit, with a teraquop footprint nearly $3\times$ lower at $p = 10^{-3}$. (✓)

In the next few sections, we review the dynamic circuit approach and the Floquet code, introduce our dynamic circuit, and explain each bullet point above. We conclude with some indications of potential future work.

PREVIOUS WORK: DYNAMIC CIRCUITS IN THE SURFACE CODE

As an introduction to dynamic circuits and their circuit-level fault distance, we review a dynamic circuit for the unrotated surface code given in [10]. This circuit uses two layers of gates to shrink stabilizers into single-body Pauli operators and measure them, then runs the circuit in reverse to restore the surface code state, as illustrated in Fig 1. While half the stabilizers shrink and are measured, the other half grow. To measure all the stabilizers, we re-run a shifted version of this circuit to

measure the remaining half.

We consider two features of this circuit: its spatial distance d , and its timelike distance d_t . Because some stabilizers become larger as the circuit runs, the spatial distance of a dynamic circuit may be reduced, as error strings can travel faster between larger stabilizers. In addition, two-qubit gates directly connect data qubits, so an elementary two-qubit gate error on $CX_{i,j}$ like $Z_i Z_j$ affects two data qubits. For the unrotated surface code these faster errors only occur diagonally and thus don't reduce the distance; however, if we tried to use this circuit on the rotated surface code [16], the spatial distance would be halved.

As for the timelike distance, we note that the standard circuit measures all stabilizers in four gate layers and one measurement layer (see, e.g., [7]), while the dynamic circuit only measures half the stabilizers in the same depth. Naively, one might think the dynamic circuit requires double the circuit depth to reach a timelike distance d_t compared to the standard circuit. However, there is a subtle distinction between the two circuits: The standard circuit compares the value of the stabilizer at time t to the value at time $(t - 1)$ to detect errors, while the dynamic circuit compares the value of the stabilizer to the single-qubit reset operation that initialized that stabilizer in the previous timestep. As a result, while we only measure the stabilizers half as often in the time-dynamic circuit, they effectively provide twice as much information, and we can reach distance d_t in the same circuit depth.

A REVIEW OF THE FLOQUET CODE

The Floquet code [5] is illustrated in Fig. 2 [5, 14, 15]. Qubits are arranged at the vertices of a periodic honeycomb lattice with horizontal and vertical dimensions L_1 and L_2 , respectively. Each cell of the lattice corresponds to a six-qubit stabilizer, given by $\otimes^6 X / \otimes^6 Y / \otimes^6 Z$ for red/green/blue cells.

Rather than directly measuring the stabilizers of the Floquet code, we deduce their value by measuring a set of gauge operators that commute with all stabilizers. Each lattice bond corresponds to a two-qubit gauge operator, given by $XX/YY/ZZ$ for red/green/blue bonds. We repeatedly measure the XX , YY , and ZZ gauge operators in sequence. The product of the gauge operators around a cell then gives the value of that stabilizer. This allows us to deduce the stabilizer values without directly performing six-qubit measurements.

A subtlety arises when considering logical operators in the Floquet code. For any given logical degree of freedom, no single representative of that logical operator commutes with all gauge operators. As a result, we have to modify the representative of the logical operator at each time step, multiplying it by gauge operators

that have just been measured to form a new representative that commutes with the next gauge operators. We illustrate this process for one horizontal and one vertical logical operator in 2. Note that while the measurement cycle has period 3, the logical operator representatives have period 6.

In this paper, we consider the Floquet code on a torus to avoid properly treating boundaries; however, it is also possible to define planar Floquet codes [15, 17]. Since our code is on a torus, it encodes two logical qubits; however, we restrict our attention to a single logical qubit since only one logical qubit survives when introducing boundaries.

STANDARD VS DYNAMIC CIRCUIT FOR THE FLOQUET CODE

We present two circuits for measuring the gauge operators, the standard ancilla-based circuit and our new dynamic one, illustrated in Fig. 3. The standard circuit requires one qubit per gauge operator, while the dynamic one requires no ancilla qubits and operates by shrinking the gauge operator onto a single qubit and measuring that qubit directly. Note that the dynamic circuit measures *every* XX operator at the measurement layer, just as in the standard circuit. This is in contrast to the case of the surface code, where switching to the dynamic circuit meant we could only measure half as many operators at once (made up for getting twice as much information per measurement). In the Floquet code, we get the advantage of improved measurements without increasing the number of gates; this is the source of improved performance.

We note that individual errors in the standard circuit only flip neighboring stabilizers, as can be seen from the evolution of the stabilizers in the top of Fig. 3. However, the dynamic circuit causes next-nearest-neighbor stabilizers to touch (see the middle columns of Fig. 3), so that individual errors can flip next-nearest-neighbors as well. This difference is illustrated in the last panel of Fig. 3, from which it follows that the standard (dynamic) circuit requires $(L_1, L_2) = (d, 2d)$ ($(L_1, L_2) = (2d, 3d)$) [18]. The qubit number for a distance- d code is then $5d^2$ for the standard circuit, vs $6d^2$ for the dynamic circuit.

To understand the logical error rate and spacetime overhead per logical operation, we must also consider the timelike distance d_t , since a braiding [7, 19–21] or lattice surgery [22–24] operation requires $d_t \approx d$. The timelike distance of our dynamic circuit is *increased* due to the improved measurements; the standard circuit requires measuring $\{XX, YY, ZZ\}$ $4d_t/3$ times, while the dynamic circuit requires only d_t . Our dynamic circuit thus requires fewer measurements per logical operation. However, every layer of our dynamic circuit must be executed sequentially, meaning a full cycle takes time

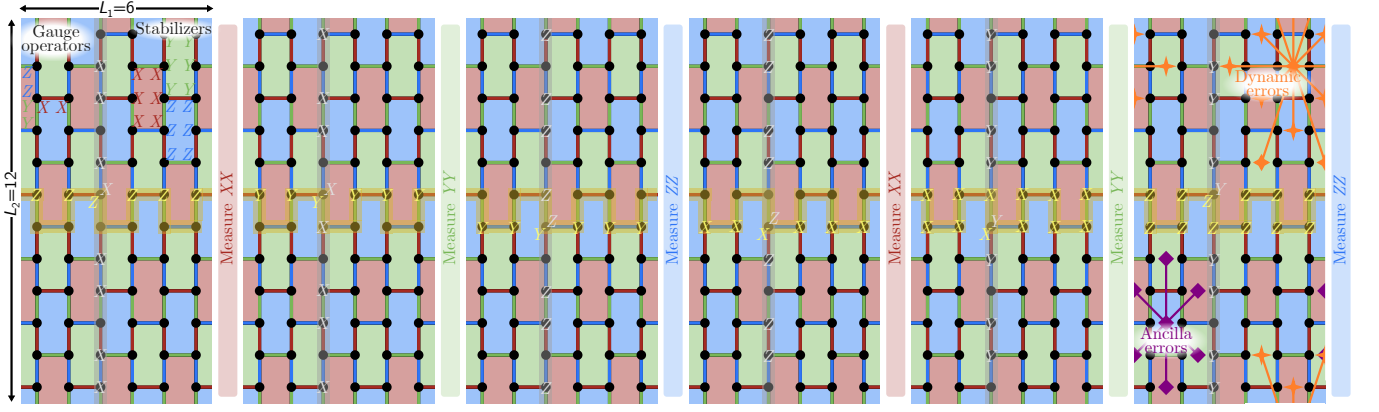


FIG. 2. An illustration of an $L_1 \times L_2$ patch of Floquet code defined on a torus. On the rightmost panel, we illustrate the gauge operators and stabilizers of the Floquet code. The Floquet code has six-qubit Pauli stabilizers around each hexagon, with red/green/blue hexagons denoting $\otimes^6 X/\otimes^6 Y/\otimes^6 Z$ stabilizers. It has two-qubit gauge operators on each bond which commute with all stabilizers, with red/green/blue bonds denoting $XX/YY/ZZ$ gauge operators. Rather than directly measure the stabilizers, we sequentially measure the $XX/YY/ZZ$ gauge operators, with the product of the gauge operators around each hexagon giving the value of the corresponding stabilizer. There is no single representative of the logical operators that commutes with all gauge operators; instead, at each step, we multiply the current representative by the previous gauge operators to create a new representative that commutes with the next gauge operators. We show a horizontal (yellow) and vertical (gray) observable as they evolve through time. In the last panel, we illustrate pairs of stabilizers that can be flipped by a single physical error for the standard (purple) and dynamic (orange) circuits. In the standard circuit, errors flip neighboring pairs of stabilizers, while in the dynamic circuit they may flip next-nearest-neighbors.

$(6t_{\text{gate}} + 3t_{\text{meas}} + 3t_{\text{reset}})$. This contrasts with the standard circuit, in which the first layer of gates to measure YY commutes with the last layer of gates to measure XX , and measured qubits do not need to be immediately reset. The standard circuit can therefore be compressed; in [14] they provide a circuit that takes amortized time $(3t_{\text{gate}} + 3\max[t_{\text{meas}}, t_{\text{reset}}])$ provided the hardware can execute measure and reset operations in parallel. As a result, depending on the hardware constraints, a logical operation in the dynamic circuit may still be slower.

For our simulations, we will compare the logical error rates of the dynamic and standard circuits at the same $d = d_t$, noting that the dynamic circuit requires slightly more qubits and the standard circuit requires slightly more measurements.

NUMERICAL RESULTS

Fig. 4 gives our simulation results using a standard depolarizing noise model (see Appendix). We record the error rate of a single pair of horizontal/vertical logical operators; the logical error rate is given by the sum of the error probabilities for these two operators. The dynamic circuit has a threshold of $\approx .29\%$, compared to $\approx .21\%$ for the standard circuit. Related to the higher threshold, the logical error rate of the distance- d dynamic circuit has a significantly lower error rate; approximately $6\times$ lower at $d = 6$, $50\times$ lower at $d = 12$, and $400\times$ lower at $d = 18$. For each curve, the exponent of the logical

error rate is slightly larger than $\lceil \frac{d}{2} \rceil$; this indicates that for the range of error probabilities p we simulate there are higher-distance errors that contribute significantly to the logical error rate.

A common figure of merit for comparing codes is the overhead required to reach the *teraquop regime* [14], the number of qubits needed to incur a 10^{-12} error probability while reaching a timelike distance $d_t = d$. Extrapolating our simulations to larger d assuming the logical error rate decays exponentially, for $p = 10^{-3}$ we require $d = 28$ for the dynamic circuit versus $d = 52$ for the standard circuit. This corresponds to 4700 qubits for the dynamic circuit and 13500 qubits for the standard circuit.

CONCLUSION

We have demonstrated that our dynamic circuit increases the threshold and lowers the resource overhead of the Floquet code. Our work leaves open a few avenues for future exploration.

First, we have neglected to introduce boundaries in our circuits [15, 17], although we do not expect boundaries to significantly affect our results. We also have not simulated a stability experiment [27] to verify that the timelike error improves similar to the spacelike error rates. We also only simulated a simple depolarizing error model; it is likely that the relative advantage changes for other qubit-specific error models, and becomes even more significant for models that include leakage.

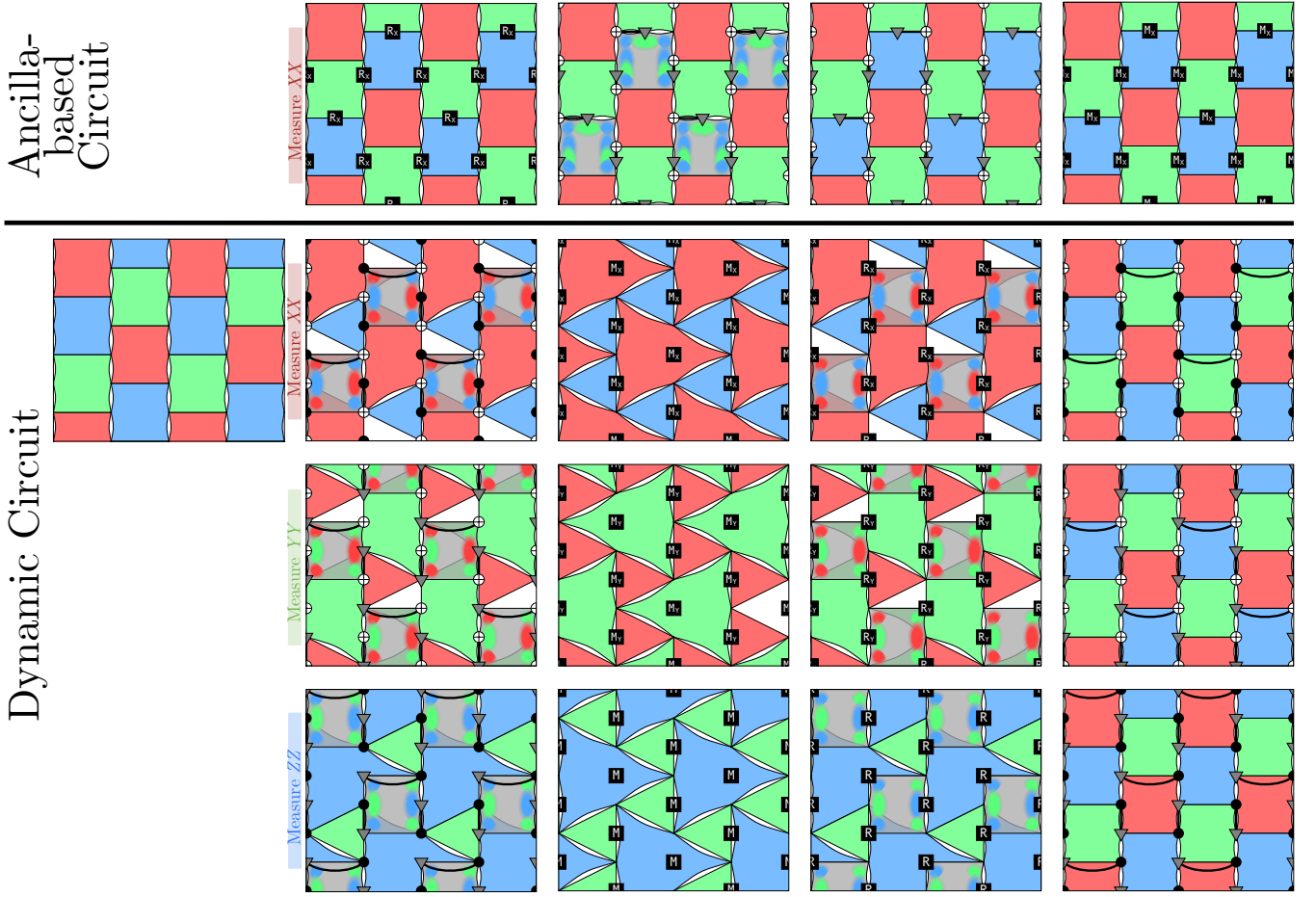


FIG. 3. Top: An ancilla-based circuit for measuring the XX gauge operators. We put one ancilla on each XX bond. The circuits for YY and ZZ are similar. Bottom: Three gauge measurements in the dynamic circuit. We measure XX gauge operators by shrinking them to a single qubit, which we then measure. We measure YY and ZZ gauge operators similarly, alternating the measured qubits to remove leakage. In the next set of gauge measurements, we reverse the target and control of each gate and continue the alternating measurement pattern. Both circuits have the same number of two-qubit gates, resets, and measurements.

In addition, our simulations were decoded using minimum-weight perfect-matching (MWPM) [6]. It has been previously shown [14, 15] that a correlated decoder [28] can reduce the teraquop footprint of the Floquet code significantly compared to MWPM. It is an open question how an improved decoder would change the relative advantage of the dynamic circuit.

Finally, numerous generalizations of the Floquet code have been introduced that also reduce stabilizer measurements to a series of two-qubit gauge measurements [29–37]; it is an open question if these codes could also benefit from our dynamic approach.

Acknowledgments—The ancilla-based simulations were performed using code included with [14]. The dynamic simulations also made substantial use of tools included in that code base.

Data availability—Stim circuits and simulation data are available at [38].

Appendix A: Noise Model

To be consistent with previous work [14, 15], we use the standard depolarizing noise model. The noise model consists of

- Single-qubit gates are followed by a single-qubit depolarizing channel with strength p .
- Two-qubit gates are followed by a two-qubit depolarizing channel with strength p .
- Idle qubits during single or two-qubit gates incur a single-qubit depolarizing channel with strength p .
- Initialization in $|0\rangle$ instead prepares $|1\rangle$ with probability p , and similar for $|+\rangle$.
- Measurement results are flipped with probability p .

Note that while our simulations of the dynamic and the standard circuits included idle errors, idle errors are significantly more damaging to the dynamic circuit, because once the standard circuit is compacted it has very few

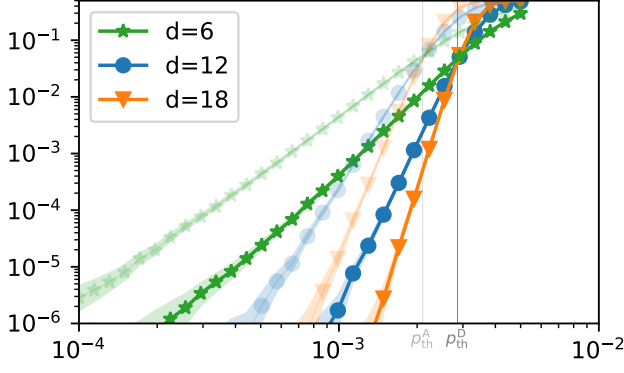


FIG. 4. Logical error rates for the dynamic circuit (bold) and standard circuit (faded) for various circuit-level distances, where the logical error rate is the sum of the logical error rate of the horizontal and vertical observable. Estimated thresholds for the standard and dynamic circuits, p_{th}^A and p_{th}^D , are shown with horizontal lines. The dynamic circuit demonstrates significant improvement in both threshold and logical error rate. Simulations performed with Stim [25] and decoded with PyMatching [26].

locations where idle errors can occur. If the dominant errors were only two-qubit gate errors, measurement errors, and reset errors, the advantage of the dynamic circuit would increase.

Appendix B: Additional numerical results

Here, we include a plot of our extrapolation of logical error rate as a function of distance, used to compute the teraquop footprint for $p = 10^{-3}$. We also include graphs of the separate horizontal and vertical logical error rates, rather than summed as in the main text. Note that the V logical error probability is the probability that the vertical logical operator is incorrect, i.e. the probability that an undetected horizontal logical operator has been applied, and similarly for the H logical error probability. The larger V logical error probability for the standard circuit was also seen in [15].

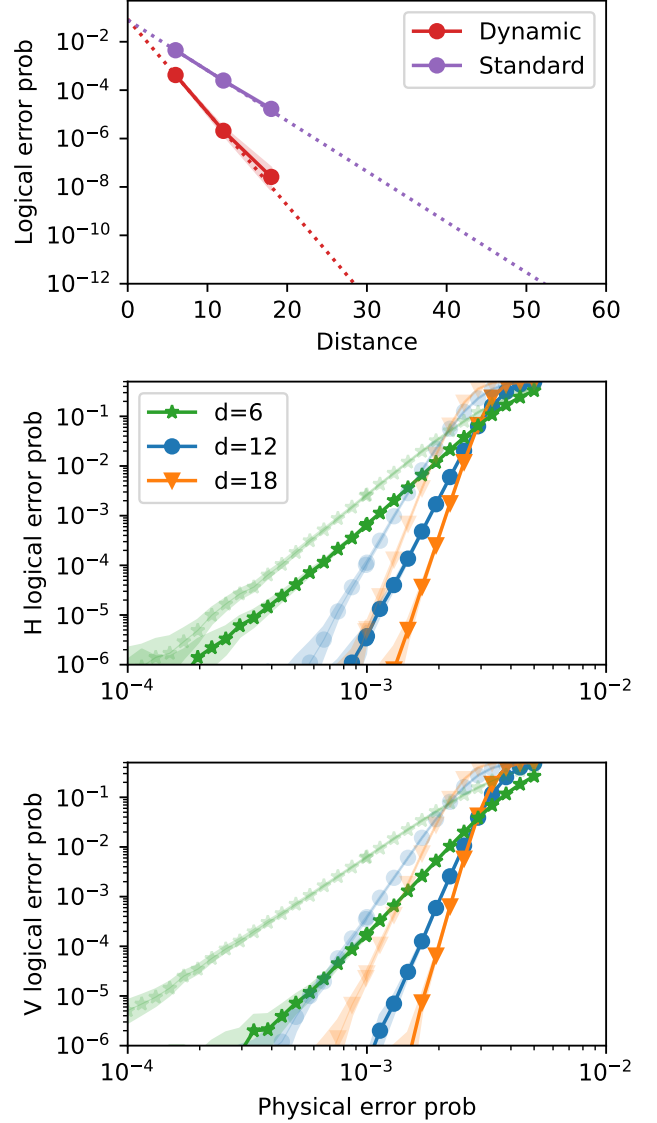


FIG. 5. Additional numerical results, including our extrapolation to the teraquop regime for $p = 10^{-3}$ and the logical error rates separated into horizontal and vertical error rates.

-
- [1] D. Gottesman, Stabilizer Codes and Quantum Error Correction, arXiv preprint arXiv:quant-ph/9705052 (1997).
 - [2] D. Poulin, Stabilizer Formalism for Operator Quantum Error Correction, Physical Review Letters **95**, 230504 (2005).
 - [3] D. Bacon, Operator Quantum Error Correcting Subsystems for Self-Correcting Quantum Memories, Physical Review A **73**, 012340 (2006).
 - [4] A. Y. Kitaev, Quantum computations: algorithms and error correction, Russian Mathematical Surveys **52**, 1191 (1997).

- [5] M. B. Hastings and J. Haah, Dynamically generated logical qubits, Quantum **5**, 564 (2021).
- [6] E. Dennis, A. Kitaev, A. Landahl, and J. Preskill, Topological quantum memory, Journal of Mathematical Physics **43**, 4452 (2002).
- [7] A. G. Fowler, M. Mariantoni, J. M. Martinis, and A. N. Cleland, Surface codes: Towards practical large-scale quantum computation, Physical Review A—Atomic, Molecular, and Optical Physics **86**, 032324 (2012).
- [8] C. Chamberland and M. E. Beverland, Flag fault-tolerant error correction with arbitrary distance codes, Quantum **2**, 53 (2018).
- [9] C. Gidney and C. Jones, New circuits and an open source decoder for the color code, arXiv preprint arXiv:2312.08813 (2023).

- [10] M. McEwen, D. Bacon, and C. Gidney, Relaxing hardware requirements for surface code circuits using time-dynamics, *Quantum* **7**, 1172 (2023).
- [11] A. Eickbusch, M. McEwen, V. Sivak, A. Bourassa, J. Atalaya, J. Claes, D. Kafri, C. Gidney, C. W. Warren, J. Gross, *et al.*, Demonstrating dynamic surface codes, arXiv preprint arXiv:2412.14360 (2024).
- [12] M. H. Shaw and B. M. Terhal, Lowering connectivity requirements for bivariate bicycle codes using morphing circuits, *Physical review letters* **134**, 090602 (2025).
- [13] D. M. Debroy, M. McEwen, C. Gidney, N. Shutty, and A. Zalcman, Luci in the surface code with dropouts, arXiv preprint arXiv:2410.14891 (2024).
- [14] C. Gidney, M. Newman, A. Fowler, and M. Broughton, A fault-tolerant honeycomb memory, *Quantum* **5**, 605 (2021).
- [15] C. Gidney, M. Newman, and M. McEwen, Benchmarking the planar honeycomb code, *Quantum* **6**, 813 (2022).
- [16] Y. Tomita and K. M. Svore, Low-distance surface codes under realistic quantum noise, *Physical Review A* **90**, 062320 (2014).
- [17] J. Haah and M. B. Hastings, Boundaries for the honeycomb code, *Quantum* **6**, 693 (2022).
- [18] Note that an earlier paper [14] misstated the vertical circuit distance, as was noted in a later paper by some of the same authors [15].
- [19] R. Raussendorf and J. Harrington, Fault-tolerant quantum computation with high threshold in two dimensions, *Physical review letters* **98**, 190504 (2007).
- [20] R. Raussendorf, J. Harrington, and K. Goyal, Topological fault-tolerance in cluster state quantum computation, *New Journal of Physics* **9**, 199 (2007).
- [21] A. G. Fowler, A. M. Stephens, and P. Groszkowski, High-threshold universal quantum computation on the surface code, *Physical Review A—Atomic, Molecular, and Optical Physics* **80**, 052312 (2009).
- [22] D. Horsman, A. G. Fowler, S. Devitt, and R. Van Meter, Surface code quantum computing by lattice surgery, *New Journal of Physics* **14**, 123011 (2012).
- [23] D. Litinski and F. von Oppen, Lattice surgery with a twist: Simplifying clifford gates of surface codes, *Quantum* **2**, 62 (2018).
- [24] A. G. Fowler and C. Gidney, Low overhead quantum computation using lattice surgery, arXiv preprint arXiv:1808.06709 (2018).
- [25] C. Gidney, Stim: a fast stabilizer circuit simulator, *Quantum* **5**, 497 (2021).
- [26] O. Higgott and C. Gidney, Sparse blossom: correcting a million errors per core second with minimum-weight matching, *Quantum* **9**, 1600 (2025).
- [27] C. Gidney, Stability experiments: The overlooked dual of memory experiments, *Quantum* **6**, 786 (2022).
- [28] A. G. Fowler, Optimal complexity correction of correlated errors in the surface code, arXiv preprint arXiv:1310.0863 (2013).
- [29] A. Paetznick, C. Knapp, N. Delfosse, B. Bauer, J. Haah, M. B. Hastings, and M. P. da Silva, Performance of planar Floquet codes with majorana-based qubits, *PRX Quantum* **4**, 010310 (2023).
- [30] A. Townsend-Teague, J. M. de la Fuente, and M. Kesselring, Floquetifying the colour code, arXiv preprint arXiv:2307.11136 (2023).
- [31] M. Davydova, N. Tantivasadakarn, and S. Balasubramanian, Floquet codes without parent subsystem codes, *PRX Quantum* **4**, 020341 (2023).
- [32] B. Rodatz, B. Poór, and A. Kissinger, Floquetifying stabiliser codes with distance-preserving rewrites, arXiv preprint arXiv:2410.17240 (2024).
- [33] Z. Zhang, D. Aasen, and S. Vijay, The X-cube Floquet code, arXiv preprint arXiv:2211.05784 (2022).
- [34] A. Dua, N. Tantivasadakarn, J. Sullivan, and T. D. Ellison, Engineering 3d Floquet codes by rewinding, *PRX Quantum* **5**, 020305 (2024).
- [35] J. C. M. de la Fuente, J. Old, A. Townsend-Teague, M. Rispler, J. Eisert, and M. Müller, XYZ ruby code: Making a case for a three-colored graphical calculus for quantum error correction in spacetime, arXiv preprint arXiv:2407.08566 (2024).
- [36] O. Higgott and N. P. Breuckmann, Constructions and performance of hyperbolic and semi-hyperbolic Floquet codes, *PRX Quantum* **5**, 040327 (2024).
- [37] A. Fahimniya, H. Dehghani, K. Bharti, S. Mathew, A. J. Kollár, A. V. Gorshkov, and M. J. Gullans, Fault-tolerant hyperbolic Floquet quantum error correcting codes, arXiv preprint arXiv:2309.10033 (2023).
- [38] J. Claes, Stim circuits and simulation results for "A dynamic circuit for the honeycomb Floquet code", [10.5281/zenodo.15854678](https://doi.org/10.5281/zenodo.15854678) (2025).